ORIGINAL ARTICLE

Investigation of Movement and Deposition Behaviors of Solid Particles in Hydraulic Water Reservoir via the CFD-DEM Coupling Method

Mandi Li[1], Decai Kong[1], Qi Guo[1], Xiangyu Liu[1], Jing Yao[1,2]*, Jianjun Hu[3] and Lijuan Chen[4]

Abstract

Solid contamination existing as solid particles in power fluid transmission systems may lead to transmission performance reduction, system failures, and component damage. The hydraulic reservoir will deposit the contamination and store hydraulic fluid. To investigate its purification ability for solid contamination, experiments and simulations for the motion and deposition status of the typical hydraulic system particles are carried out to reveal the interaction of particles and fluid in hydraulic water reservoirs. The results show that the CFD-DEM coupling method could predict the accurate deposition position of iron particles and sand particles when ignoring the small-scale turbulence effect in the flow field. Besides, the particle motion traces and deposition patterns in the reservoir illustrate that the flow development on the bottom surface results in the particles turning, and particles tend to settle in the low flow energy position. The motion of particles is also linked to particles Stokes number, and the same-size sand particles are easily driven by the fluid. The contribution of this paper could provide a guide for predicting the particle motion and deposition pattern in the hydraulic reservoir.

Keywords: Solid contamination, CFD-DEM simulation, Motion and deposition of solid particles, Hydraulic reservoir, Visualization experiment

1 Introduction

The solid contamination is unavoidably mixed in power fluid transmission flow. It will bring side effects to the hydraulic system, such as transmission performance degradation, system failure, and components' life span shortening [1]. As an accessory in the transmission, the hydraulic reservoir could sediment solid contamination and provide a clean working fluid medium. Therefore, hydraulic reservoir purification capacity should be studied to remove particle pollutants conductively and specifically.

To this end, the status of solid contamination should be known for the reservoir deposition analysis in the hydraulic system. Usually, contamination varies in materials, sizes, and shapes. However, they could still be classified into metal particles, including iron, aluminum, copper, etc., and non-metal particles, including dust, sand, rubber, etc., by their sources. The sizes of these solid particles range from 50 to 500 μm [2], and the shapes of the particles are diverse from spherical, polyhedron, flake, and other forms [3]. In this case, the sedimentation of particles could be complex in the hydraulic reservoir, and the flow field pattern with purification ability should be unveiled.

So far, researchers have initially analyzed the sedimentation of solid particles in hydraulic reservoirs. Muttenthaler et al. [4] used three-phase CFD simulations to investigate the particle accumulation in the hydraulic reservoir. They found that the accumulation status of different size particles changes with the oil flow rate and geometry of the reservoir. Besides, the accumulation of

*Correspondence: jyao@ysu.edu.cn

[1] School of Mechanical Engineering, Yanshan University, Qinhuangdao 066004, China
Full list of author information is available at the end of the article

Li *et al. Chinese Journal of Mechanical Engineering*   (2022) 35:118

Page 2 of 12

the particles depending on the bottom flow status also has been found [5]. Yao et al. [6] used the discrete phase model (DPM) to simulate the contamination separation rates for iron and rubber particles in a newly designed reservoir. Even though these papers have investigated the particle contamination accumulation status in the hydraulic reservoir, the particle contamination motion procedure is less concerned.

Among the research on hydraulic reservoirs, simulation analysis on particle sedimentation status has been the most prevalent. The DPM is used primarily to simulate the trajectory of particles in the flow field [7–9]. However, the DPM might ignore the collisions of particle-wall and particle-particle [10–12]. Since the DPM pays more attention to the tracking of particle trajectory, the final position for particle deposition cannot be visually displayed in simulation results easily, which is hard to compare with the actual particle deposition situation.

The computational fluid dynamics-discrete element method (CFD-DEM) coupling method has been gradually applied to the simulation analysis for the particle status in the flow field. It could expertly describe shapes, sizes, forces and motions of particles [13–15]. For example, Chu et al. [16] used this method to analyze the influence of distinctive size particles on the medium flow in a dense medium cyclone. Wu et al. [17] utilized the CFD-DEM coupling method to accurately discuss the movement of particles in solid-liquid mixing devices with different structures. Kuang et al. [18] reviewed the related research on the CFD-DEM coupling method in pneumatic transportation. They proposed that this method has significant advantages in analyzing transportation distances for different particle sizes and shapes. In future work, complex wall constraints are essential for improving particle sedimentation efficiency in the optimization design of hydraulic reservoir structures. Hence, the collision effect of particles cannot be ignored, and the CFD-DEM coupling method is a good choice to simulate the particle status.

Therefore, to simulate and evaluate the pattern of particle motion in the hydraulic reservoir, the CFD-DEM coupling method is used in this paper. Besides, the visualization experiments for particle deposition are also compared with simulation. For the convenience of visualization, the flow medium of the power fluid transmission system in this paper is water.

For the arrangement of the contents in this paper, the experiment setup and particle sedimentation results are introduced first. Then, the CFD-DEM coupling method is illustrated, and the simulation validation with the experiment results is conducted. After that, the particle movement and deposition analysis with flow characteristics are discussed by the numerical simulation to reveal the contamination accumulation pattern in the hydraulic reservoir.

2 Experiment Setup and Results
2.1 Experiment Setup
The particle deposition visualization experiment is firstly proposed in this paper to explore particle deposition patterns. The diagram of the experiment is shown in Figure 1. It consists of a camera, a transparent model, a throttle valve, soft pipes, a pump, a frequency transducer, a water tank and a flowmeter.

The experiment would study the deposition of two types of particles representing metal and non-metal solid contamination commonly existing in the power fluid transmission systems. Considering the feasibility of the experiment and the appearance possibility of the particle contamination in hydraulic systems, 500 μm-diameter uniform iron balls represent metal particle contamination, and white quartz sands with sizes ranging from 20 mesh to 40 mesh represent non-metal particle contamination in experiments. A transparent reservoir model is built to study particle sedimentation, which takes the single-baffle hydraulic reservoir as a reference. The model made from polymethyl methacrylate material has a 30 L volume, and its length-width-height ratio is designed according to the requirements of the hydraulic reservoir. A blue background paper is pasted on the bottom surface of the reservoir to observe the movement and deposition of particles as well as further image post-process.

In the experiment, the pump lifts the water-particle mixed fluid into the reservoir model. The pump frequency transformer controls the fluid flow rate to maintain the reservoir inlet flow speed at 1.24 m/s. The liquid

Figure 1 Diagram of particle deposition experiment device
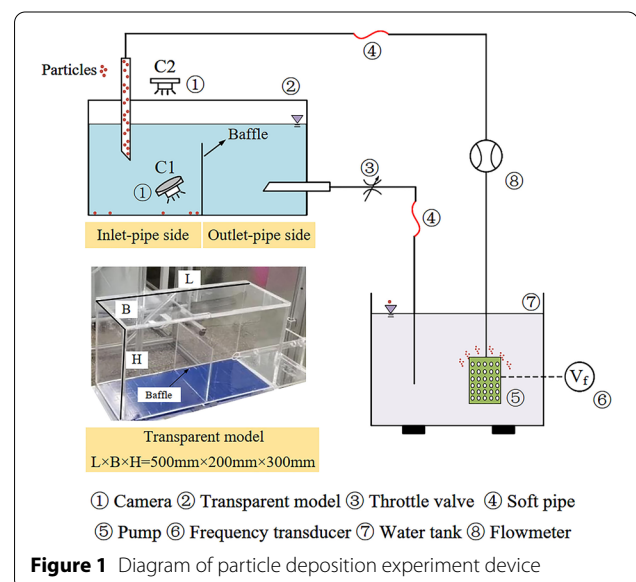
level is kept 400 mm above the model bottom by adjusting the throttle valve during the experiment. When particles roll at the bottom surface of the reservoir, particle movement will be captured by the camera at the C1 position shown in Figure 1. After particles stay stable, they will deposit on the bottom of the reservoir. Then, images of the particle deposition area are taken at the C2 position shown in Figure 1.

2.2 Experimental Results
After the experiment for iron and sand particles, the sedimentation situation for the two types of particles was processed by MATLAB to eliminate noise from light reflections on the water surface.

Since a baffle exists in the middle of the reservoir model, the bottom of the reservoir surface is separated into two parts. The bottom surface with the inlet pipe is called the inlet-pipe side, and the bottom surface with the outlet pipe is called the outlet-pipe side. From the particle deposition experiment results, iron and sand particles are all deposited on the inlet-pipe side of the reservoir, and there is no deposition on the outlet-pipe side of the reservoir. Therefore, the experiment results shown in this paper are only particle deposition conditions on the inlet-pipe side of the reservoir. Due to the symmetrical structure of the reservoir, the deposition states of particles on both sides of the central axis are similar. Therefore, half deposition images of iron and sand particles on the inlet-pipe side are jointed in Figure 2. The yellow dashed lines represent the distribution boundary of the particle deposition, and they surround the most deposited particles.

By comparing the deposition status of two types of particles in Figure 2, two types of particles are all scattered, presenting an arc-like distribution near the baffle. They are also aggregated at the two corners of the reservoir. Besides, sand particles are closer to the wall or baffle side than iron particles, and the distribution area of sand particles is more extensive.

3 Numerical Model
3.1 Solving Process
To analyze the movement and deposition of solid particles in the reservoir, the CFD-DEM coupling method is implemented in this study. The flow field is simulated by ANSYS Fluent$^{©}$, and the particle motion is simulated by EDEM$^{©}$. The CFD-DEM coupling simulation schematic diagram is shown in Figure 3.

In the coupling process, fluid in the reservoir is regarded as the continuous phase, and particles are regarded as the discrete phase. Fluent simulates the transient flow field by solving the time-averaged Navier-Stokes equation with the SST k-ω model until the steady state. Then, the coupling calculation of particle motion and flow field is started. The
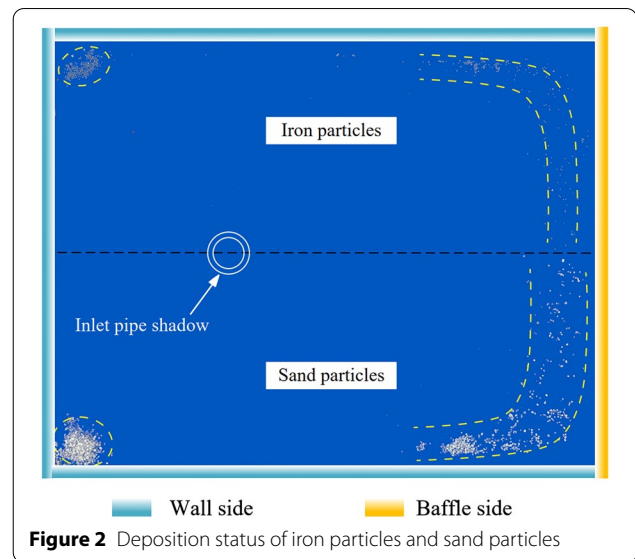

Figure 2 Deposition status of iron particles and sand particles

forces calculated in the flow field on particles are transmitted to EDEM. It will update the speed and position information of particles and then transfer the reverse force from particles to the flow field. This process will be repeated on the next time step until the final time step is completed.

3.2 CFD Model
In this case, the fluid is assumed to be isothermal and incompressible. The continuity and momentum equations for the fluid phase are given as follows:

$$\frac{\partial \rho_f}{\partial t} + \nabla \cdot (\rho_f \boldsymbol{u}_f) = 0, \tag{1}$$

$$\frac{\partial (\rho_f \boldsymbol{u}_f)}{\partial t} + \nabla \cdot (\rho_f \boldsymbol{u}_f \boldsymbol{u}_f) = -\nabla p + \nabla \cdot \boldsymbol{\tau} + \rho_f \boldsymbol{g} + \boldsymbol{F}_s, \tag{2}$$

where ρ_f, $\boldsymbol{u}_f$, p, $\boldsymbol{\tau}$, and $\boldsymbol{g}$ indicate fluid density, fluid velocity, pressure, stress component, and gravitational acceleration. In addition, $\boldsymbol{F}_s$ represents the interaction term that involves the effect of the forces on particles.

3.3 DEM Model
In the DEM model, the translational motion and rotational motion of a particle can be described according to Newton's laws of motion [19, 20], which are:

$$m_p \frac{\mathrm{d}\boldsymbol{u}_p}{\mathrm{d}t} = \boldsymbol{F}_f + \sum \boldsymbol{F}_c, \tag{3}$$

$$I_p \frac{\mathrm{d}\boldsymbol{\omega}_p}{\mathrm{d}t} = \sum \boldsymbol{T}_c, \tag{4}$$
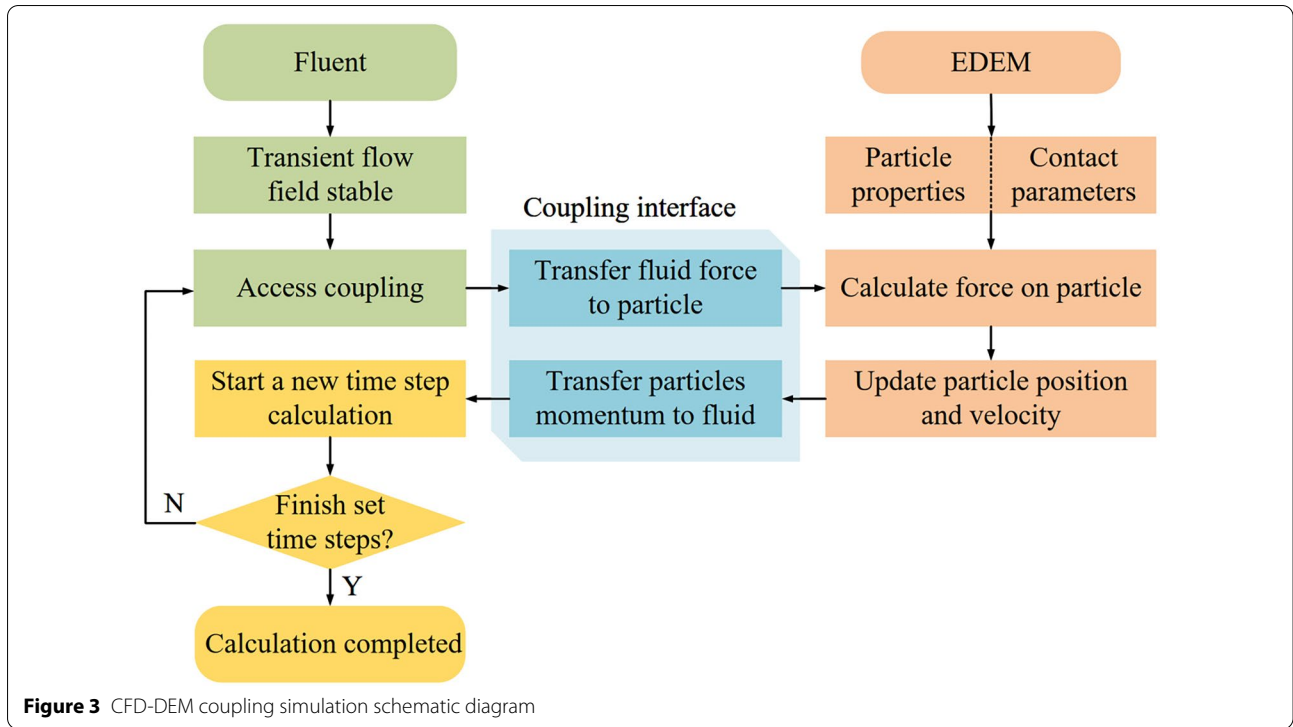
Figure 3 CFD-DEM coupling simulation schematic diagram

where m_p, $\boldsymbol{u}_p$, I_p, and $\boldsymbol{\omega}_p$ indicate particle mass, particle velocity, inertia tensor, and rotational velocity, respectively.

The fluid force on the particle $\boldsymbol{F}_f$ is given by:

$$\boldsymbol{F}_f = \boldsymbol{F}_G + \boldsymbol{F}_B + \boldsymbol{F}_P + \boldsymbol{F}_{Drag} + \boldsymbol{F}_{VR} + \boldsymbol{F}_{Saff}, \tag{5}$$

where $\boldsymbol{F}_G$, $\boldsymbol{F}_B$, $\boldsymbol{F}_p$, $\boldsymbol{F}_{Drag}$, $\boldsymbol{F}_{VR}$, and $\boldsymbol{F}_{Saff}$ indicate gravity, buoyancy force, pressure gradient force, drag force, virtual mass force, and Saffman force.

The contact force $\boldsymbol{F}_c$ includes the normal and tangential component, which is given by:

$$\boldsymbol{F}_c = \boldsymbol{F}_{c,n} + \boldsymbol{F}_{c,t}, \tag{6}$$

where $\boldsymbol{F}_{c,n}$ is normal contact force, and $\boldsymbol{F}_{c,t}$ is a tangential contact force.

The contact torque $\boldsymbol{T}_c$ is generated by tangential contact force and rolling friction, which is given by:

$$\boldsymbol{T}_c = \boldsymbol{T}_t + \boldsymbol{T}_r, \tag{7}$$

where $\boldsymbol{T}_t$ is tangential contact torque, and $\boldsymbol{T}_r$ is generated by rolling friction.

3.4 Fluid-solid Interaction Force

There are several types of interaction forces between fluid and particles such as buoyancy force, pressure gradient force, drag force, virtual mass force, and Saffman force.

These interaction forces are given by:

$$\boldsymbol{F}_p = -\frac{1}{6}\pi d_p^3 \frac{\partial \boldsymbol{p}}{\partial x}, \tag{8}$$

$$\boldsymbol{F}_{Drag} = \frac{1}{8}C_D \pi d_p^2 \rho_f \left(\boldsymbol{u}_f - \boldsymbol{u}_p\right)^2, \tag{9}$$

$$C_D = \frac{24}{Re} \cdot \left(1 + 0.15 \cdot Re^{0.687}\right), \tag{10}$$

$$Re = \frac{\rho_p d_p \left|\boldsymbol{u}_f - \boldsymbol{u}_p\right|}{\mu}, \tag{11}$$

$$\boldsymbol{F}_{VR} = -\frac{1}{2}V_p \rho_f \frac{\mathrm{d}\boldsymbol{u}_p(t)}{\mathrm{d}t}, \tag{12}$$

$$\boldsymbol{F}_{Saff} = 1.61(\mu \rho_f)^{1/2}\left(\frac{d_p}{2}\right)^2 \left(\boldsymbol{u}_f - \boldsymbol{u}_p\right)\left|\frac{\mathrm{d}\boldsymbol{u}_f}{\mathrm{d}y}\right|, \tag{13}$$

where C_D, d_p, V_p, ρ_p, μ, and Re indicate drag factor, particle diameter, particle volume, particle density, fluid kinetic viscosity, and Reynolds number.

3.5 Particle Size and Shape Distribution Description

As fundamental physical parameters of particles, particle size and shape could affect the motion of particles and the interaction between particles and fluid. Therefore, it

Li *et al. Chinese Journal of Mechanical Engineering*   (2022) 35:118

Page 5 of 12

is essential to consider the actual shape and size of particles in the simulation [21].

Two hundred iron particles and sand particles samples in the experiment are randomly selected to represent the shape and size of the particles. Then, multiple SEM photographs are taken to observe the details of particles.

The typical SEM photographs for iron particles and sand particles are shown in Figure 4(a). The shape and size of iron particles are regular and uniform; their particle diameter is 500 μm. However, sand particles have various sizes and shapes. Hence, an average statistical method combined with projection is used to describe sand particles since the size and shape distribution of particles follow the normal distribution [22].

Figure 4(b) shows that the shape of sand particles is mainly cuboid. The aspect ratio can describe the two-dimensional shape of those particles. Its statistical mean value is 1.3 for quartz sand [22]. Due to the shape diversity of sand particles and the coarse size in Section 2.1., it is not facile to directly correspond with the DEM model. Therefore, photograph measurement results and projection area equality are used to represent the size of sand particles.

As the projection area equality is shown in Figure 5, the fitted rectangular area is equivalent to the actual projected area of sand particles. l and w indicate the best-fit length and width of sand particles. A matching circle is constructed to maintain the area equality with the fitted rectangular. The diameter of the circle is evaluated, which matches the normal distribution.

Among the SEM photographs shown in Figure 4(b), the largest and smallest sand particles in this image are taken as the up and down limit of the particle size to evaluate the matching circle equivalent diameter d_e. It is subject to the normal distribution, which is:

$$d_e \sim N(830, 150^2)\mu m. \tag{14}$$

Model particle diameter d_m distribution in EDEM for sand particles could be conducted from the aspect ratio and circle diameter d_e, which is:
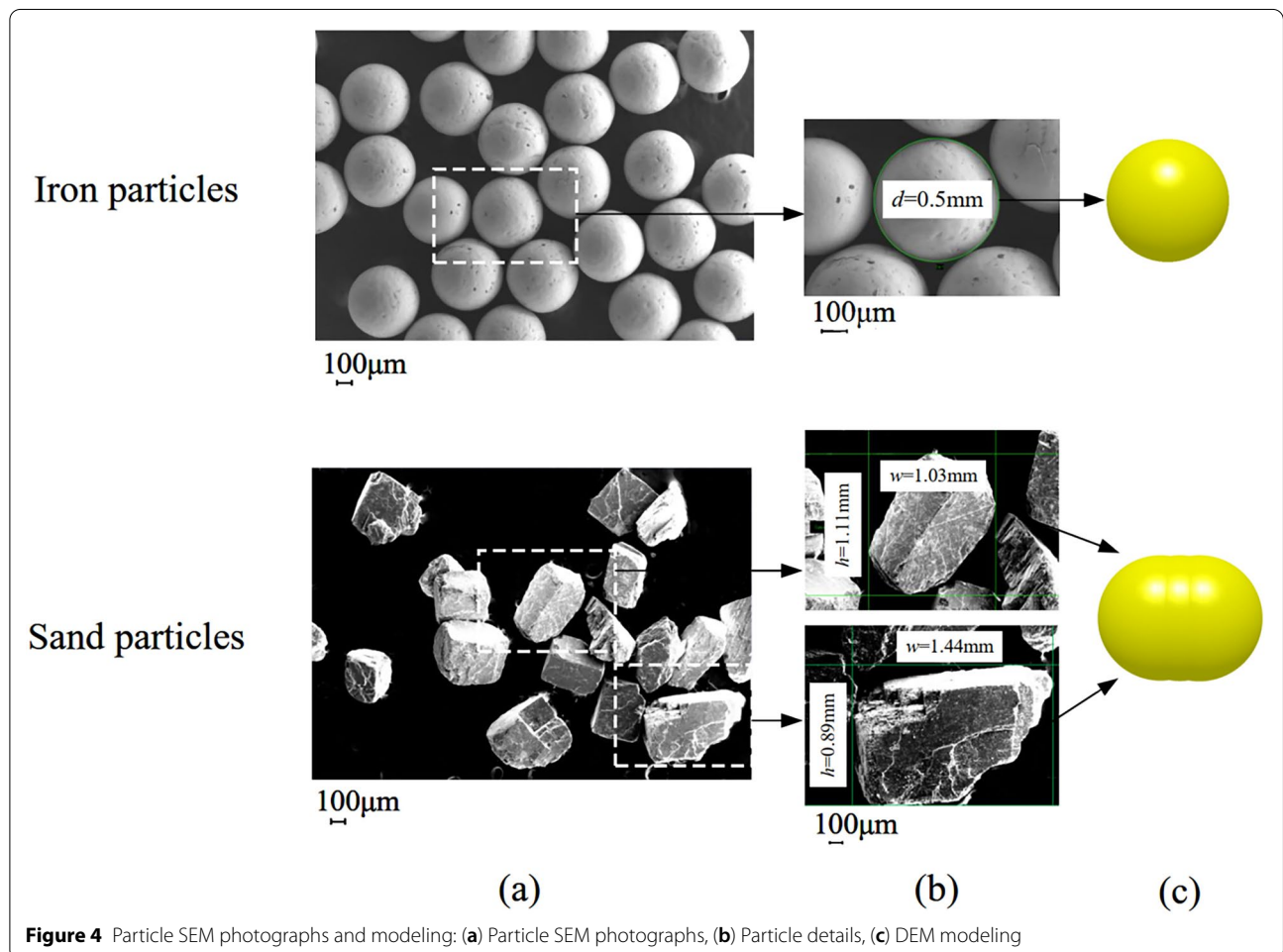

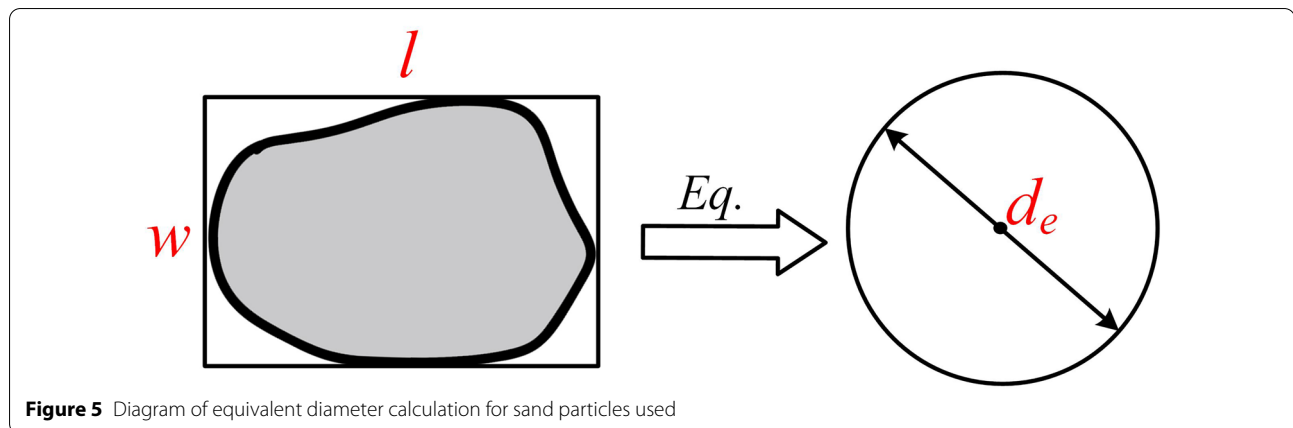**Figure 4** Particle SEM photographs and modeling: (**a**) Particle SEM photographs, (**b**) Particle details, (**c**) DEM modeling

Li *et al. Chinese Journal of Mechanical Engineering*   (2022) 35:118

Page 6 of 12

Figure 5 Diagram of equivalent diameter calculation for sand particles used

$$d_{\mathrm{m}} \sim N(645, 117^2)\mu\mathrm{m}. \tag{15}$$

The iron and sand particles models are consequently established in EDEM, shown in Figure 4(c).

3.6 Stokes Number

Particle properties for following the fluid could be measured by Stokes number. It is the ratio of particle relaxation time and flow characteristic time [23]. When Stokes number is more significant, the time for particles to respond to flow is longer, which means the particles have a weaker ability to follow the fluid flow. The expression of Stokes number is:

$$St = \frac{\tau_{\mathrm{p}}}{\tau_{\mathrm{f}}} = \frac{\rho_{\mathrm{p}} d_{\mathrm{p}}^2 \boldsymbol{u}_\infty}{18\mu L}, \tag{16}$$

where τ_{p}, τ_{f}, $\boldsymbol{u}_\infty$, and L indicate particle relaxation time, flow characteristic time, flow characteristic velocity, and flow characteristic length.

3.7 Simulation Setup

The structured CFD mesh of the reservoir fluid domain is shown in Figure 6. The liquid-particle mixing fluid flows into the inlet pipe and out of the outlet pipe to the water tank. Therefore, the inlet boundary condition is defined as a velocity-inlet condition of 1.24 m/s, and the outlet boundary condition is set as an outflow condition. The upper surface of the liquid in the reservoir is not restrained. As a result, the boundary condition for the upper surface of the model is set as symmetry. According to the experimental situation, the rest parts of the model are selected as the wall boundary condition.

Besides, it is essential to verify the grid independence of the reservoir flow field so that the grid number does not affect simulation accuracy [24]. By monitoring and recording the outlet flow data under different grid numbers, grid independence is guaranteed with the 4 mm grid size and the total of 1482233 grid numbers.

According to the experiment, the material of the reservoir model is polymethyl methacrylate. As a result, the wall material properties in EDEM include density (2500 kg·m^{-3}), Poisson's ratio (0.25), and shear modulus (2.2×10^8 Pa). Because the particles flowing into the reservoir in experiments have a random direction and random velocity, the dynamic particle factory is defined on the inlet plane of the flow field. The particle's release speed from the dynamic particle factory is set from 1 m/s to 1.5 m/s in random directions. Excepting parameters of particles and model, other the DEM setting parameters for iron and sand particles are listed in Table 1 [25–28].

In the CFD-DEM coupling simulation, the particle phase mesh does not affect the liquid phase mesh. EDEM mesh is used for particle tracking and retrieval, which affects the simulation speed. EDEM grid size is generally set to 3–5 times particle radius to maintain particle simulation accuracy [29]. In this work, the grid size is set to be three times particle radius to ensure simulation accuracy. Furthermore, the time step in Fluent should be greater than the EDEM time step. Typically, the time step in Fluent should be an integral multiple of time step in EDEM to capture the collision in particle motion [30]. In this work, the time step in Fluent is set to be 100 times the time step of EDEM. The total number of particles is 2000 until the particles are settled. The details of simulation parameter settings are shown in Table 2.

4 Particle Movement and Deposition Analysis
4.1 Comparison between Simulation and Experiment
The simulation validation is crucial to confirm the accuracy of simulation results. In the paper, the validation is
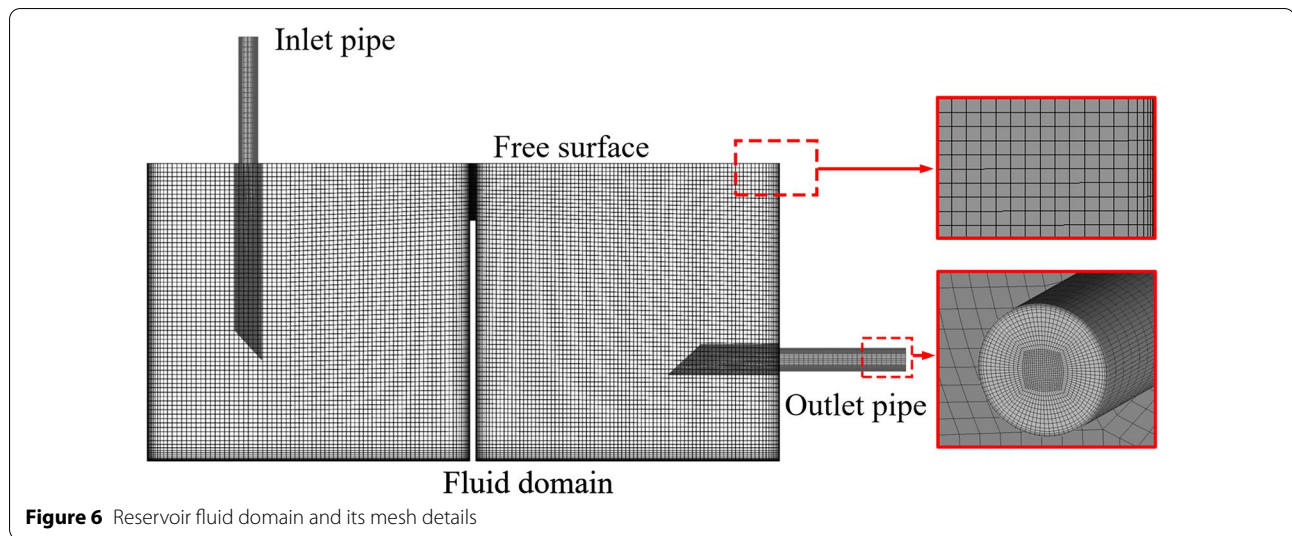
Figure 6 Reservoir fluid domain and its mesh details

Table 1 EDEM particle simulation parameters

Property	Iron	Sand
Diameter(μm)	500	380–1280
Poisson's ratio	0.3	0.4
Density(kg·m^{-3})	7800	1600
Shear modulus(Pa)	7×10^{10}	2.13×10^{7}
Particle-particle coefficient of restitution	0.5	0.44
Particle-particle static friction coefficient	0.15	0.27
Particle-particle rolling friction coefficient	0.01	0.01
Particle-wall coefficient of restitution	0.629	0.48
Particle-wall static friction coefficient	0.14	0.268
Particle-wall rolling friction coefficient	0.015	0.02

Table 2 Coupling parameters of Fluent and EDEM

Case	Fluent time step(s)	EDEM time step(s)	EDEM grid size(mm)
Iron	1×10^{-4}	1×10^{-7}	0.625
Sand	2×10^{-4}	2×10^{-6}	0.970

by comparing the deposition area of particles from simulation and experiment.

The particles remain stable at the end of the simulation. Therefore, the situation of iron and sand particles from the simulation could be regarded as deposition, as shown in Figure 7(a). The experimental result of the particle is shown in Figure 7(b). The simulation shows that both iron and sand particles are accumulated on two corners of the left side of the inlet pipe shadow. They all show an arc-like distribution on the other side of the pipe shadow.
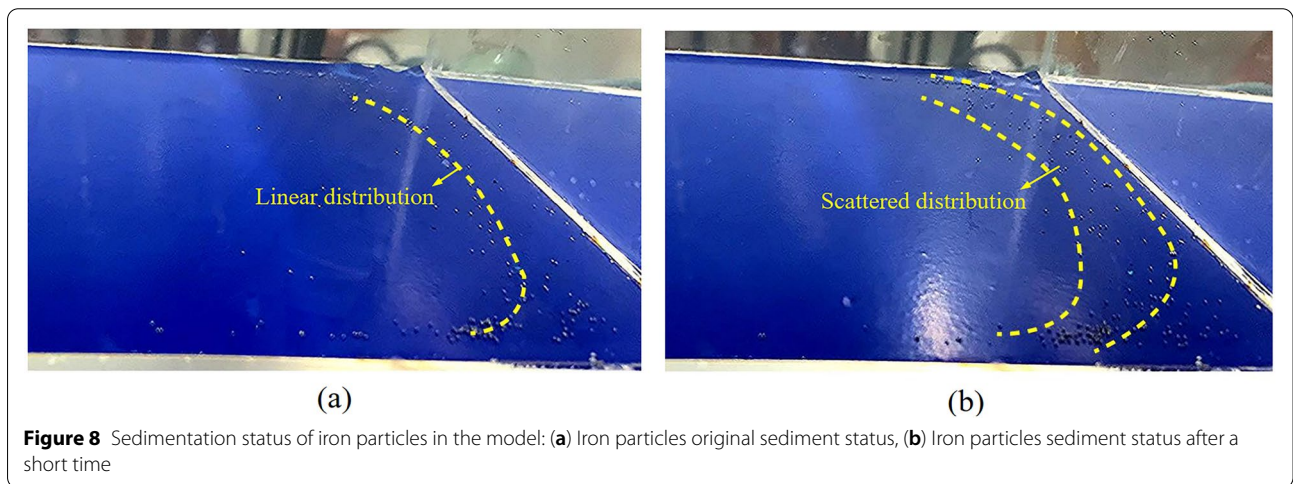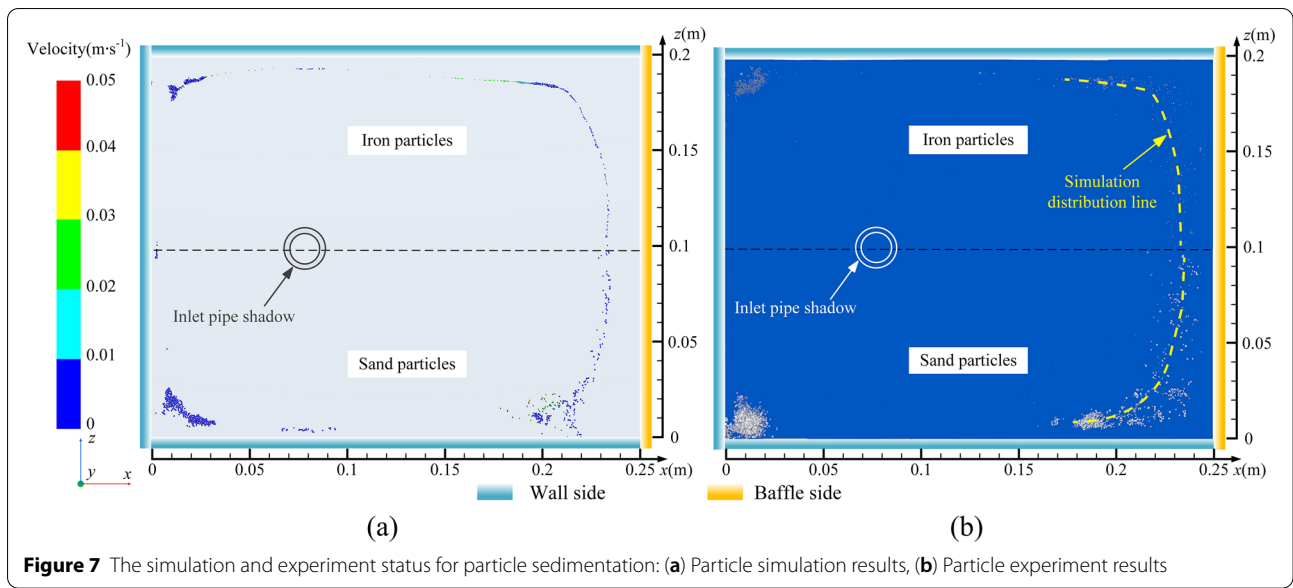
By comparison, the accumulation status of iron and sand particles in the simulations is similar to the experimental results.

However, the scattered distribution phenomenon of particles on the right side existing in the experiment result is not reflected in the simulation status. To explore the reason, the movement of iron particles in the right area of the inlet pipe is photographed by the camera in the C1 position, as shown in Figure 8. Yellow dash lines could illustrate the particle distribution status.

As can be seen in Figure 8(a), firstly, the particles present a linear distribution like the simulation when they just reach the deposition position near the baffle. After a short time, the particles are driven by the small-scale turbulence in the flow, which disturbs the linear distribution of particles, and forms a scattered distribution, as shown in Figure 8(b). Since the Reynolds time-averaged and SST *k-ω* model are used in the flow simulation, the time-varying small-scale turbulence cannot be reflected in the simulation [31]. Even though the sedimentation of the right-side particles in simulation could not show the scatter distribution, the simulated particle line is in the range of experimental particle distribution. Therefore, the CFD-DEM coupling model is regarded as accurately predicting particle deposition location.

4.2 Relationship between Particle Deposition Position and Flow Field

The particle deposition and movement status should first be studied for reservoir contamination analysis. The deposition position and movement trajectory of particles in the model are shown in Figure 9(a), where the upper half is the iron particles' motion status, and the lower half is the sand particles' motion status. For analyzing

Figure 7 The simulation and experiment status for particle sedimentation: (**a**) Particle simulation results, (**b**) Particle experiment results

Figure 8 Sedimentation status of iron particles in the model: (**a**) Iron particles original sediment status, (**b**) Iron particles sediment status after a short time

convenience, the bottom surface is divided into several areas according to the different movement trajectory of particles, including the transition area ①③ where the particles do not settle, the deposition area ②④ where particles are locally accumulated, and the direct motion area ⑤ where the particles are finally in an arc-like distribution.

Since the particle deposition position is related to the velocity of the flow field, this paper further analyzes the relationship between particle deposition position and the bottom surface velocity of the model.

Figure 9(b) shows the composition of iron particle deposition position and x-velocity contour with partial streamline. In *Areas a* and *b*, the velocities stagnation

and streamlines convergence situation happen, as shown by the magenta dotted line. This line exists where the x-velocity direction changes, that is $v_x = 0$. Furthermore, deposition area ② and direct motion area ⑤ for particle deposition are also near magenta dotted lines. But deposition area ④ is far from the line.

To explore the relationship between the deposition status of particles and other velocities status, this work analyzes the x-velocity v_x, the z-velocity v_z, and the velocity magnitude v at Line M and N, depicted in Figure 10. According to the velocity situation, the particles accumulate in the position owning to a local minimum velocity magnitude. The v_x and v_z directions also change
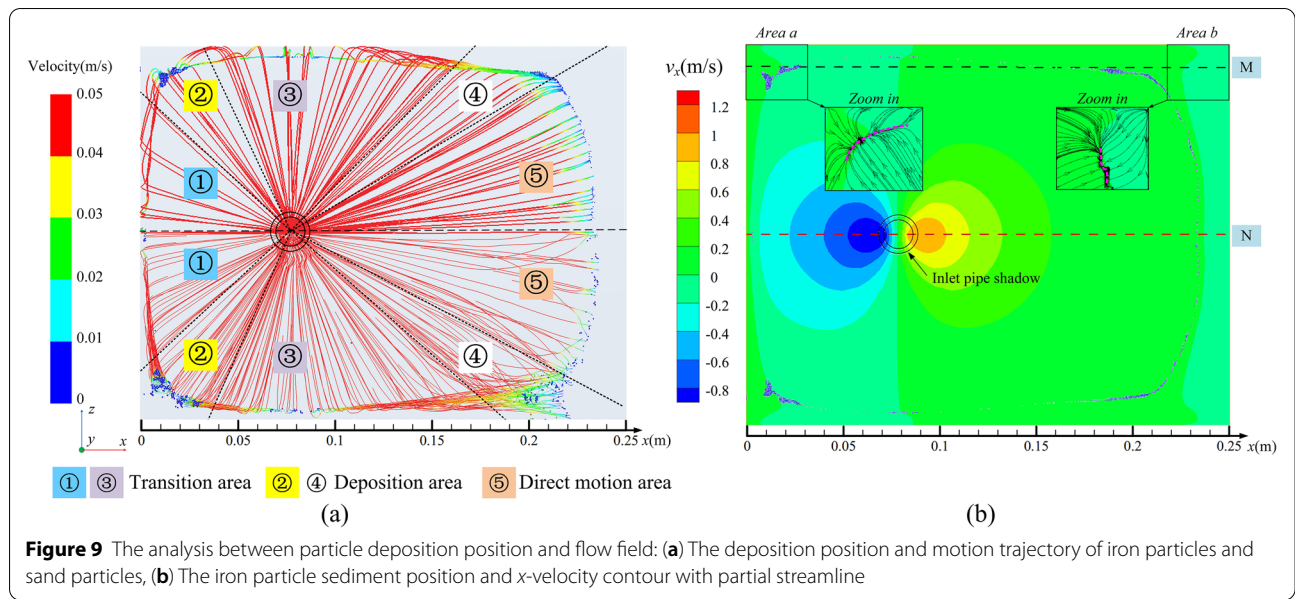
Li *et al. Chinese Journal of Mechanical Engineering*   (2022) 35:118

Page 9 of 12

Figure 9 The analysis between particle deposition position and flow field: (**a**) The deposition position and motion trajectory of iron particles and sand particles, (**b**) The iron particle sediment position and *x*-velocity contour with partial streamline
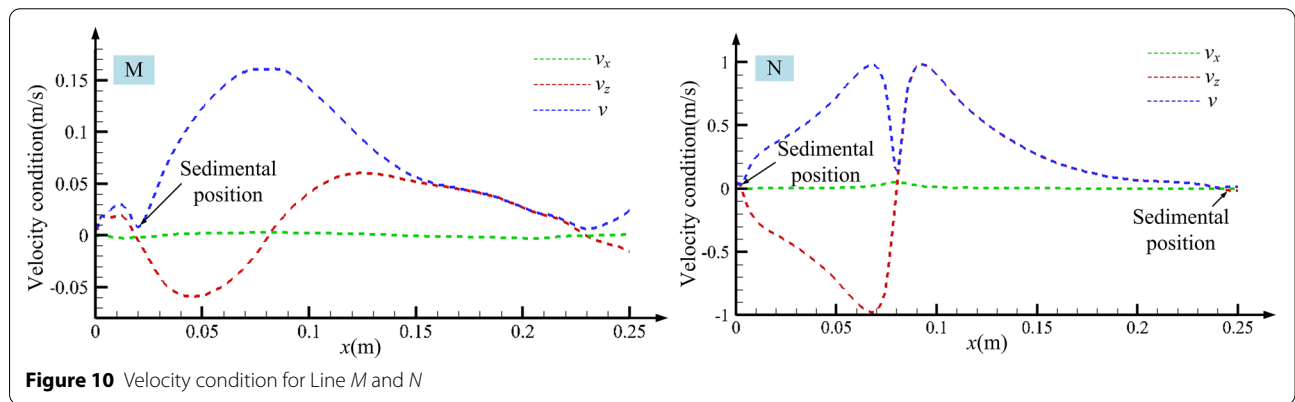

Figure 10 Velocity condition for Line *M* and *N*

in the deposition area ② and the direct motion area ⑤. It indicates that particles are easy to accumulate in the lower flow energy position of the flow field.
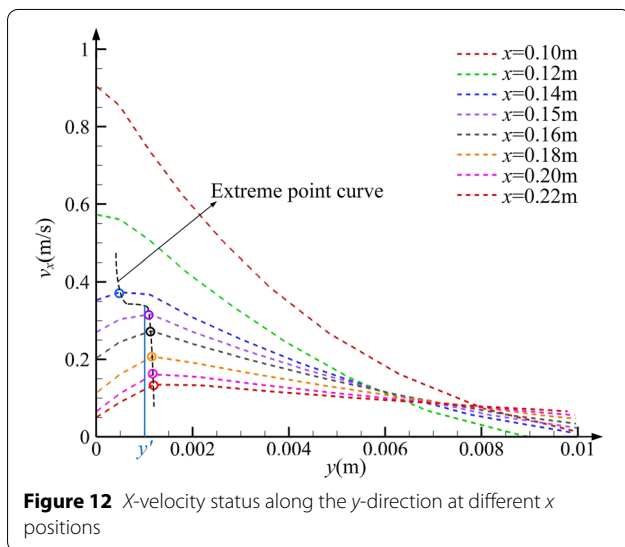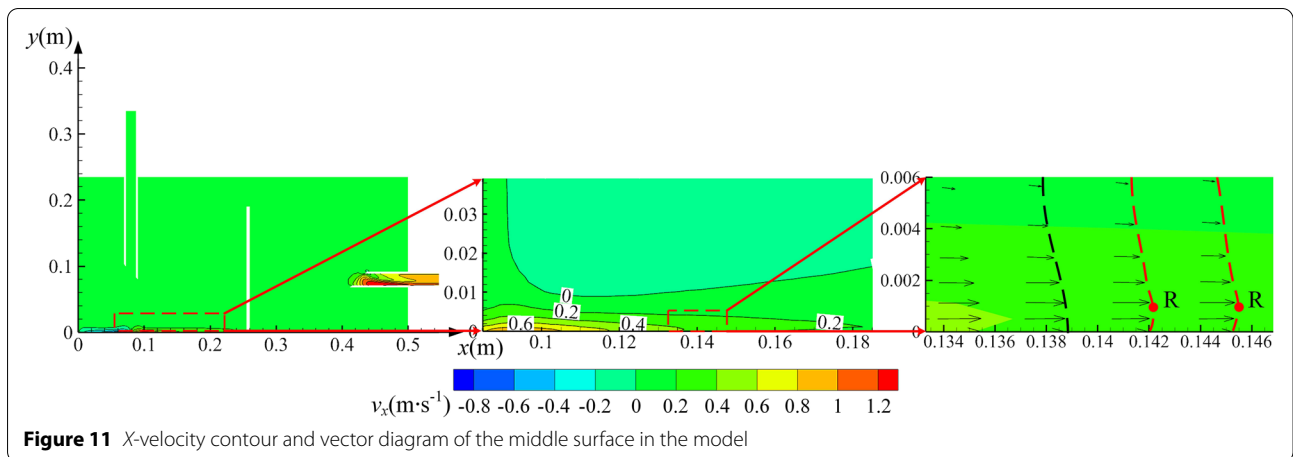
Moreover, the velocity gradient $\partial v_x/\partial x$ in the deposition area ② is greater than the direct motion area ⑤, where v_x is closer to 0. When the absolute value of $\partial v_x/\partial x$ is small, the small-scale turbulence effect could be strong and significantly interfere with particle deposition. Therefore, it indicates that the particles in the direct motion area ⑤ are more sensitive to small-scale turbulence effect than the deposition area ② in the experiment.

4.3 Iron and Sand Particles Motion Analysis

In the direct motion area ⑤, the motion trajectories of iron particles and sand particles are different in Figure 9(a). The iron particles always move in a straight line, while the sand particles first move in a straight line, then move in a curve line, and finally reach the deposition

position. The velocity properties near the bottom surface are analyzed to investigate the motion trajectories difference between the two types of particles.

Figure 11 represents the contour of *x*-velocity and vector diagram of the middle surface for the model. It can be seen that when the flow is up to the reservoir bottom, a wall jet is formed and pushes particles to move forward. In the middle surface for this simulation, the wall jet status presents as the *x*-velocity variation. On the right side of the inlet pipe, the *x*-velocity of the flow field near the bottom surface decreases and tends to be stable as the distance in *x*-direction increases, according to the contour of velocity. Besides, *x*-velocity has an extreme velocity point *R* in the *y*-direction by the vector diagram. To explore the specific height and property of *R*, the velocity change curves along the *y*-direction at different distances in the *x*-direction are shown in Figure 12.

Figure 11 X-velocity contour and vector diagram of the middle surface in the model

Figure 12 X-velocity status along the y-direction at different x positions

the extreme velocity point R moves to a higher position (larger than y') as the flow develops, going beyond the average height of particles. Since the shape of sand particles is mostly cuboid, the variation of the velocity gradient $\partial v_x/\partial y$ might cause the sand particle to flip. Consequently, its movement state is unstable, and the particle trajectory of sand is becoming curved primarily. Besides, the velocity variation from Figure 11 states the development of the wall jet on the bottom surface. The schematic diagram of the velocity v_x for sand particles in the x-direction is shown in Figure 13.

4.4 Influence of Stokes Number on Particle Deposition

The properties of particles influence the deposition status in the reservoir model as well. According to the particle movement trajectory in Figure 9(a), the difference in particle deposition locations is directly related to particle properties under the same flow state. As can also be seen in Figure 9(a), the deposition position of sand particles is closer to the wall than iron particles. In Figure 9(a), the iron particles rebound after hitting the wall in the transition area ③, then follow the flow field to deposit. In contrast, the sand particles only follow the flow field in the transition area ③ without rebounding, indicating they have smaller inertia and can follow the flow field well.
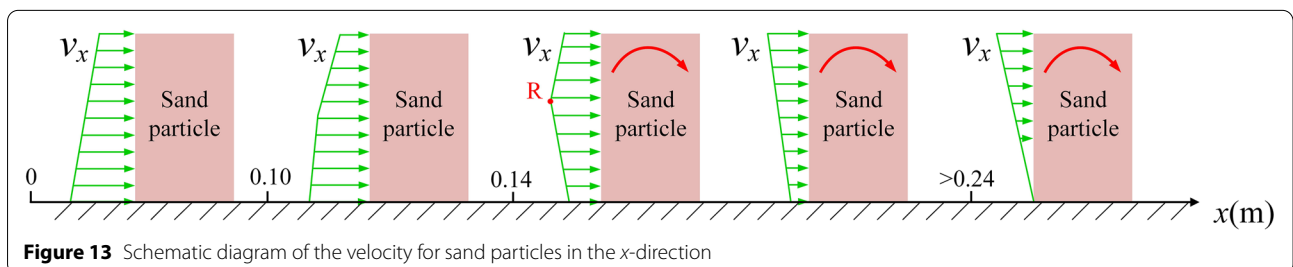
Along the x-axis, the extreme velocity point is gradually away from the bottom in the direction of the model height. When x is less than 0.14 m, v_x rapidly drops along the y-axis and almost has no extreme point. When it reaches 0.14 m, v_x first increases and then decreases along the y-axis. Meanwhile, the extreme velocity point R appears, and the height of the point is small. Afterward,

Figure 13 Schematic diagram of the velocity for sand particles in the x-direction

Li *et al. Chinese Journal of Mechanical Engineering*　　　(2022) 35:118

Page 11 of 12

Table 3 Stokes numbers of iron particles and sand particles

Property	Iron	Sand
Density(kg·m^{-3})	7800	1600
Diameter(mm)	0.5	0.83(average)
Stokes number	8.9	4.1(average)

Besides, the distance of sand particle deposition from the inlet shadow is further than that of iron particles. It implies that the minimum velocity to drive the sand particles is smaller than that of iron particles.

The ability of particles to follow fluid motion is evaluated by Stokes number. By Eq. (14), the characteristic velocity and length should be defined. Hence, in this work, the inlet velocity of the model is chosen to be the characteristic velocity, and the diameter of the inlet pipe is chosen to be the characteristic length. Stokes numbers of the two types of particles are calculated as shown in Table 3. The average Stokes number for sand particles is 4.1, and Stokes number for iron particles is 8.9. Consequently, the sand particles could follow the flow field better, consistent with the discussion results above.

5 Conclusions

In this paper, the CFD-DEM coupling method is used to simulate and predict the deposition position of particles in the hydraulic water reservoir, which considers the forces of particle-particle, particle-wall, and particle-flow field. Furthermore, the visualization experiment of the movement and accumulation of the particles in the reservoir is designed. The comparison of simulation and experiment shows that this method has high accuracy in predicting the deposition position of particles in the flow field.

In addition, the location of particle deposition and the relationship between particle motion trajectory and flow velocity are revealed through particle motion trajectory analysis. The non-circular particles in the direct motion area first move in a straight line and then move in a curve line, where the height of the extreme velocity point at the bottom of the reservoir is greater than the particle diameter. Meanwhile, the movement of different particles in the same flow field is analyzed, and it is found that sand particles with a smaller Stokes number follow the flow field more strongly. In addition, the relationship between the deposition position of particles and the flow field is analyzed, and it is concluded that particles tend to accumulate near the position with low flow energy.

Furthermore, at the particle deposition position where the flow field velocity and velocity gradient are small, the small-scale turbulence in the actual flow field significantly impacts the final particle deposition position,

while the simulation using the SST k-ω turbulence model is challenging to reflect accurate minor turbulence. This paper could provide a guide for predicting the particle motion and deposition pattern in the hydraulic reservoir.

Author contributions
JY was in charge of the whole trial; ML did data analysis and wrote the manuscript; DK finished the modeling and assisted with the manuscript checking, ML, DK, QG, XL, JH, and LC reviewed and edited the manuscript. All authors read and approved the final manuscript.

Authors' Information
Mandi Li, born in 1993, is currently a PhD candidate at *School of Mechanical Engineering, Yanshan University, China*. She received her master degree from *Northeastern University, China*, in 2018. Her research interests include fluid transmission and control technology.
Decai Kong, born in 1998, is currently a master candidate at *School of Mechanical Engineering, Yanshan University, China*.
Qi Guo, born in 1999, is currently a master candidate at *School of Mechanical Engineering, Yanshan University, China*.
Xiangyu Liu, born in 1997, is currently a master candidate at *School of Mechanical Engineering, Yanshan University, China*.
Jing Yao, born in 1978, is currently a professor at *Yanshan University, China*. She received her PhD degree from *Yanshan University, China*, in 2009. Her research interests include fluid power and control.
Jianjun Hu, born in 1982, is currently a professor at *Yanshan University, China*. He received his PhD degree from *Yanshan University, China*, in 2015. His research interests include flow measurement and flow display technology.
Lijuan Chen, born in 1989. is currently an experimenter at *Nanjing Institute of Technology, China*. She is currently a doctoral candidate with *Shihezi University, China*. Her current research interests are intelligent hydraulic wind power, electro-hydraulic servo system and fault diagnosis of hydraulic valve.

Author Details
[1]School of Mechanical Engineering, Yanshan University, Qinhuangdao 066004, China. [2]Fluid Power Transmission and Control Laboratory, Yanshan University, Qinhuangdao 066004, China. [3]School of Civil Engineering and Mechanics, Yanshan University, Qinhuangdao 066004, China. [4]School of Mechanical Engineering, Nanjing Institute of Technology, Nanjing 211167, China.

References
[1] L Wu, K Chen, Y Guo. Research on cavitation phenomena in pilot stage of jet pipe servo-valve with a rectangular nozzle based on large-eddy simulations. *AIP Advances*, 2019, 9(2): 025109.
[2] ISO 4406. *Hydraulic Fluid power—fluids—method for coding the level of contamination by solid particles*. Geneva, Switzerland: International Standards Organization, 1999.
[3] X Liu, H Ji, W Min, et al. Erosion behavior and influence of solid particles in hydraulic spool valve without notches. *Engineering Failure Analysis*, 2020, 108: 104262.
[4] L Muttenthaler, B Manhartsgruber. *Prediction of particle resuspension and particle accumulation in hydraulic reservoirs using three-phase*

Li *et al. Chinese Journal of Mechanical Engineering*   (2022) 35:118

Page 12 of 12

CFD simulations//fluid power systems technology. American Society of Mechanical Engineers, 2019, 59339: V001T01A008.

[5] L Muttenthaler, B Manhartsgruber. Euler-Lagrange CFD simulation and experiments on accumulation and resuspension of particles in hydraulic reservoirs. *Journal of the Brazilian Society of Mechanical Sciences and Engineering*, 2020, 42(4): 1-17.

[6] J Yao, X Liu, M Li, et al. Design and characteristic analysis of miniaturized labyrinth hydraulic reservoir. *Journal of Mechanical Engineering*, 2021, 57(24): 83-92. (in Chinese)

[7] Chang P, Xu G, Huang J. Numerical study on DPM dispersion and distribution in an underground development face based on dynamic mesh. *International Journal of Mining Science and Technology*, 2020, 30(4): 471-475.

[8] V Tič, D Lovrec. Air-release and solid particles sedimentation process in a hydraulic reservoir. *Tehnički Vjesnik*, 2013, 20(3): 407-412.

[9] B Bozzini, M E Ricotti, M Boniardi, et al. Evaluation of erosion–corrosion in multiphase flow via CFD and experimental analysis. *Wear*, 2003, 255(1-6): 237-245.

[10] C Kloss, C Goniva, G Aichinger, et al. Comprehensive DEM-DPM-CFD simulations-model synthesis, experimental validation and scalability// Proceedings of the seventh international conference on CFD in the minerals and process industries, CSIRO, Melbourne, Australia. 2009: 9-11.

[11] J Chen, Y Wang, X Li, et al. Reprint of "Erosion prediction of liquid-particle two-phase flow in pipeline elbows via CFD–DEM coupling method". *Powder Technology*, 2015, 282: 25-31.

[12] D Zeng, E Zhang, Y Ding, et al. Investigation of erosion behaviors of sulfur-particle-laden gas flow in an elbow via a CFD-DEM coupling method. *Powder Technology*, 2018, 329: 115-128.

[13] M Lungu, J Siame, L Mukosha. Comparison of CFD-DEM and TFM approaches for the simulation of the small scale challenge problem 1. *Powder Technology*, 2021, 378: 85-103.

[14] J Fang, L Wang, Y Hong, et al. Influence of solid–fluid interaction on impact dynamics against rigid barrier: CFD–DEM modelling. *Géotechnique,* 2021: 1-16.

[15] G T Nguyen, E L Chan, T Tsuji, et al. Resolved CFD–DEM coupling simulation using Volume Penalisation method. *Advanced Powder Technology*, 2021, 32(1): 225-236.

[16] K W Chu, Y Wang, Q J Zheng, et al. CFD-DEM study of air entrainment in falling particle plumes. *Powder Technology*, 2020, 361: 836-848.

[17] L Wu, M Gong, J Wang. Development of a DEM–VOF model for the turbulent free-surface flows with particles and its application to stirred mixing system. *Industrial & Engineering Chemistry Research*, 2018, 57(5): 1714-1725.

[18] S Kuang, M Zhou, A Yu. CFD-DEM modelling and simulation of pneumatic conveying: A review. *Powder Technology*, 2020, 365: 186-207.

[19] J Hu, G Xu, Y Shi, et al. The influence of the blade tip shape on brownout by an approach based on computational fluid dynamics. *Engineering Applications of Computational Fluid Mechanics*, 2021, 15(1): 692-711.

[20] L Zhou, Y Zhao. CFD-DEM simulation of fluidized bed with an immersed tube using a coarse-grain model. *Chemical Engineering Science*, 2021, 231: 116290.

[21] Q Chen, T Xiong, X Zhang, et al. Study of the hydraulic transport of non-spherical particles in a pipeline based on the CFD-DEM. *Engineering Applications of Computational Fluid Mechanics*, 2020, 14(1): 53-69.

[22] Y Wu. *Experimental study on the drag force coefficient of natural geotechnical particle materials in the liquid*. Dalian: Dalian University of Technology, 2017. (in Chinese)

[23] T C W Lau, G J Nathan. Influence of Stokes number on the velocity and concentration distributions in particle-laden jets. *Journal of Fluid Mechanics*, 2014, 757: 432-457.

[24] C Moliner, F Marchelli, N Spanachi, et al. CFD simulation of a spouted bed: Comparison between the discrete element method (DEM) and the two fluid model (TFM). *Chemical Engineering Journal*, 2019, 377: 120466.

[25] S Huang, X Su, G Qiu. Transient numerical simulation for solid-liquid flow in a centrifugal pump by DEM-CFD coupling. *Engineering Applications of Computational Fluid Mechanics*, 2015, 9(1): 411-418.

[26] S Huang, J Huang, Z Hui, et al. Wear calculation of sandblasting machine based on EDEM-FLUENT coupling. *International Journal of Hydromechatronics*, 2018, 1(4): 447-459.

[27] Li L. Two phase numerical simulation of continuous abrasive water jet system based on EDEM. *IOP Conference Series: Earth and Environmental Science*. IOP Publishing, 2020, 546(4): 042055.

[28] G K P Barrios, R M de Carvalho, A Kwade, et al. Contact parameter estimation for DEM simulation of iron ore pellet handling. *Powder Technology*, 2013, 248: 84-93.

[29] K W Chu, J Chen, B Wang, et al. Understand solids loading effects in a dense medium cyclone: Effect of particle size by a CFD-DEM method. *Powder Technology*, 2017, 320: 594-609.

[30] Y He, A E Bayly, A Hassanpour. Coupling CFD-DEM with dynamic meshing: A new approach for fluid-structure interaction in particle-fluid flows. *Powder Technology*, 2018, 325: 620-631.

[31] P R Spalart. Detached-eddy simulation. *Annual Review of Fluid Mechanics*, 2009, 41: 181-202.